

Charge Carrier Mapping for Z-scheme Photocatalytic Water Splitting Sheet by Categorization of Microscopic Time-resolved Image Sequence

Makoto Ebihara

Chuo University

Takeshi Ikeda

TOTO Ltd.

Sayuri Okunaka

Japan Technological Research Association of Artificial Photosynthetic Chemical Process (ARPChem)

Hiromasa Tokudome

Japan Technological Research Association of Artificial Photosynthetic Chemical Process (ARPChem)

Kazunari Domen

The University of Tokyo <https://orcid.org/0000-0001-7995-4832>

Kenji Katayama (✉ kkata@kc.chuo-u.ac.jp)

Chuo University <https://orcid.org/0000-0003-3278-6485>

Article

Keywords: z scheme, water splitting, photoexcited carrier dynamics, microscopy, spectral clustering

Posted Date: March 11th, 2021

DOI: <https://doi.org/10.21203/rs.3.rs-276945/v1>

License:   This work is licensed under a Creative Commons Attribution 4.0 International License.

[Read Full License](#)

Version of Record: A version of this preprint was published at Nature Communications on June 17th, 2021. See the published version at <https://doi.org/10.1038/s41467-021-24061-4>.

1 Charge Carrier Mapping for Z-scheme Photocatalytic Water 2 Splitting Sheet by Categorization of Microscopic Time-resolved 3 Image Sequence

4
5 Makoto Ebihara¹ Takeshi Ikeda,^{2,3} Sayuri Okunaka,^{2,3} Hiromasa Tokudome,^{2,3} Kazunari
6 Domen,^{4,5} and Kenji Katayama^{1*}

7 ¹ Department of Applied Chemistry, Chuo University, Tokyo 112-8551, Japan

8 ² Research Institute, TOTO Ltd., Kanagawa 253-8577, Japan

9 ³ Japan Technological Research Association of Artificial Photosynthetic Chemical Process
10 (ARPCChem), Tokyo 101-0032, Japan

11 ⁴ Research Initiative for Supra-Materials, Interdisciplinary Cluster for Cutting Edge Research,
12 Shinshu University, Nagano 380-8553, Japan

13 ⁵ Office of University Professors, The University of Tokyo, Tokyo 113-8656, Japan

14
15 *Corresponding author:

16 K. Katayama, Phone: +81-3-3817-1913, E-mail: kkata@kc.chuo-u.ac.jp

17 Abstract

18 Photocatalytic water splitting system using particulate semiconductor materials is a promising
19 strategy for converting solar energy into hydrogen and oxygen. In particular, visible-light-driven ‘Z-
20 schematic’ printable photocatalyst sheets are cost-effective and scalable systems. However, little is
21 known about the fundamental photophysical processes, which are key to explain and promote
22 photoactivity. Here, we applied the pattern-illumination time-resolved phase microscopy (PI-PM) for
23 the printed photocatalyst sheet, composed of Mo-doped BiVO₄ and Rh-doped SrTiO₃, indium tin oxide
24 (ITO) as an electron mediator, to investigate photo-generated charge carrier dynamics. Using the PI-
25 PM, we successfully observed for the first time the position- and structure-dependent charge carrier
26 behavior, including visualization of the active/inactive sites in the sheet, under the visible-light
27 irradiation via the time sequence images and the clustering analysis. This combination methodology
28 could not only lead to the maximum performance of photocatalyst sheets but also applicable to other
29 systems involving electron transfer.

30 **Keywords:** z scheme, water splitting, photoexcited carrier dynamics, microscopy, spectral clustering

32 Introduction

33 Water splitting into hydrogen and oxygen by sunlight energy is one of the most promising clean
34 energy resources in the future, and tremendous efforts have been made mostly for the development of
35 new materials,¹⁻³ and extended for the device fabrication and large-scale development.^{4,5} In the overall
36 water splitting, careful selection of the band positions is necessary both for the reduction of proton and
37 the oxidation of water, and co-catalysts are necessary to promote the reactions. New materials have
38 emerged one after another, and one of the materials which can split water using a single semiconductor
39 photocatalyst, aluminum-doped strontium titanate (SrTiO₃:Al), showed high efficiency with an
40 apparent quantum efficiency of almost 100% overall water splitting efficiency under UV light
41 illumination in 2020,⁶ and the mechanism had been studied.⁷ Alternatively, two different materials are
42 used by combination; each one is used for hydrogen and oxygen generation, and the remaining charges
43 are compensated by charge transfer between two materials, called as 'Z-scheme water splitting system.'
44 1,2,8-10

45 In the Z-scheme strategy, various combinations of two different semiconductors were introduced.
46 One of the favored combinations is BiVO₄ and Rh doped SrTiO₃ (SrTiO₃:Rh) as oxygen and hydrogen
47 generation catalysts. In the earlier stage of the Z-scheme researches, the photo-excited electrons in
48 BiVO₄ were transferred to SrTiO₃:Rh via a redox shuttle in an aqueous solution. Still, the number of
49 candidates for redox shuttles is limited, such as IO³/I, Fe²⁺/Fe³⁺. As a next step, the Z-scheme was
50 demonstrated without using the redox mediator by direct contact between BiVO₄ and SrTiO₃:Rh
51 semiconductors,¹¹ where the photo-excited electrons and holes in each photocatalyst recombine
52 directly at the interface. The conductive binders have been searched and introduced to promote charge
53 transport between two materials. Alternatively, particulate photocatalyst sheets, wherein the
54 photocatalyst particles are fixed onto a glass substrate, have been reported in recent years. For example,
55 a physical vapor deposition (PVD)-based photocatalyst sheet composed of SrTiO₃:Rh,La and
56 BiVO₄:Mo embedded in an evaporated Au layer can split water under solar light with solar-to-
57 hydrogen conversion efficiency of 1.1 %.^{12,13} Also, we have recently developed a new-type
58 photocatalyst sheet named a printable photocatalyst sheet, which can be prepared via facile and
59 extensive screen-printing method incorporating a conductive colloidal binder (e.g., Au, ITO) with a
60 highly-packed film structure.¹³⁻¹⁵ However, the STH was merely 0.4 %, ¹⁵ and it is necessary to
61 understand the electron transfer process and design the optimal film structure for achieving STH >
62 1 %.

63 In the water splitting by photocatalysts, it is essential how efficiently photo-excited charge
64 carriers are separated and utilized for water oxidation and reduction without losing them due to
65 recombination. So far, charge carrier dynamics in various photocatalyst particles and films, including
66 SrTiO₃ or BiVO₄, have been studied. Transient absorption and time-resolved photoluminescence have

67 been frequently utilized to understand the processes. Concerning SrTiO₃, various doping causes trap
68 sites, and the lifetime of the charge carriers was extended from microseconds to milliseconds, and the
69 effect was studied in relevance to the photocatalytic activity. In several reports, doping of a single
70 element induced a recombination center and reduced the charge carriers, but co-doping could suppress
71 the recombination.^{16–18} The charge carrier dynamics was also studied for BiVO₄ on the ultrafast and
72 wide time range. The effects of trap states were discussed mostly for elongation of hole lifetimes,^{19–22}
73 and the effect of active and inactive oxygen defects were clarified.²³ Also, a heterojunction of BiVO₄
74 with WO₃ was studied and revealed that the junction effectively removed electrons at the interband
75 states,²⁴ providing a benefit for water oxidation on a millisecond to second order.²⁵

76 On the other hand, our approach for studying the charge carrier dynamics uses the special
77 combination of the measurement of the refractive index change and its accompanying original analysis
78 method called spectral clustering method, instead of the absorption change or photoluminescence.^{26,27}
79 As for the former measurement approach, the monitorization via the refractive index change has merit
80 to favor the detection of the interfacial charge transfer because the limitation of the detection
81 wavelength is relaxed due to the broad wavelength response. So far, this method has been applied for
82 studying charge transfer at the interfaces of the photocatalysts²⁸ and dye-sensitized solar cells.²⁹ For
83 detecting the refractive index change, we used the transient grating (TG) method and studied the
84 dynamics of the charge carriers for TiO₂,^{30–32} and hematite photoanodes.^{33–35}

85 The charge carrier behavior depends on the local structure and is inhomogeneous in nature for
86 the photocatalysts, typically composed of calcinated particles and aggregates. Many researches have
87 been devoted for studying the spatio-temporal behavior of charge carrier dynamics by using TA and
88 photoluminescence microscopy on micro-scales,^{36–38} and the photocurrent behavior by microscopic
89 photo-electrochemical measurements.^{39,40} We also have extended our measurements of the refractive
90 index change for a local mapping of the transient responses of photo-excited charge carriers. (pattern-
91 illumination phase microscopy (PI-PM)). By illuminating a pattern of light, the sequence of images
92 due to the refractive index change was obtained, and the image quality was recovered by the image
93 recovery calculation techniques.⁴¹ The lifetime distribution of the charge carriers for a TiO₂ particulate
94 film was obtained, and the research clarified a broad range of the lifetime of charge carriers.⁴²
95 Furthermore, the local responses of charge carriers were categorized by the spectral clustering method
96 and found the hidden local responses of the non-radiative exciton relaxation for higher pump
97 intensities.⁴³ Thus, using the combination of PI-PM and the spectral clustering method, we can
98 investigate the position- and structure-dependent charge carrier behavior under light irradiation, and
99 also assign the carrier at specific positions.

100 These findings have motivated us to apply this combination of PI-PM and clustering analysis
101 method for one of the most promising Z-scheme water splitting materials, BiVO₄:Mo/SrTiO₃:Rh with
102 a conductive colloidal binder (ITO), as a printable photocatalyst sheet with a conductive colloidal

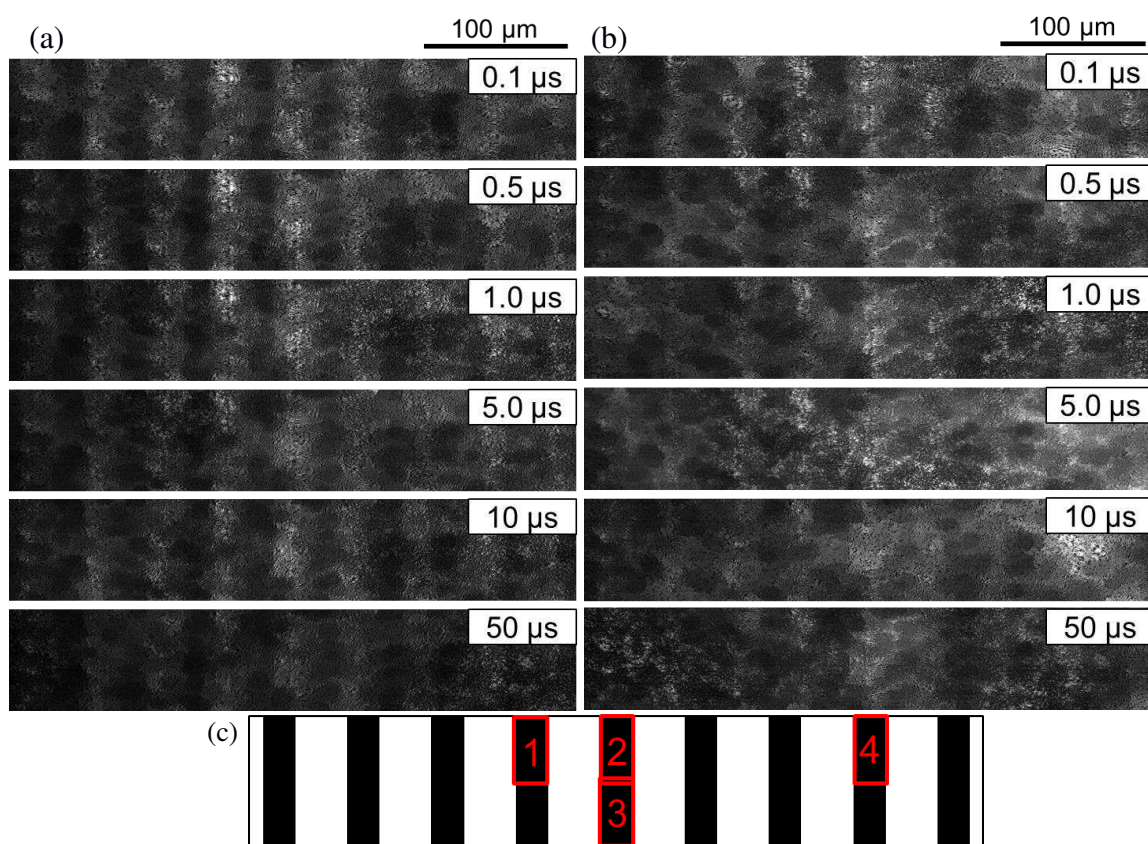
103 binder (ITO) prepared by the printing method. We could visualize the spatially-resolved photocatalytic
104 activity by the categorization of the charge carrier behaviors. This new methodology could detect the
105 real active and inactive sites in the photocatalytic device and will support the optimization of the active
106 structure of the photocatalyst.

107

108 **Result and Discussion**

109 The time-resolved experiments were performed on the visible-light responsible printed
110 photocatalyst sheet composed of SrTiO₃:Rh, BiVO₄:Mo, and ITO (STOR/ITO/BVOM) in two
111 different solvents (acetonitrile (ACN) and water). Figure 1 shows the image sequences of the refractive
112 index change for SrTiO₃:Rh/ITO/BiVO₄:Mo (STOR/ITO/BVOM) in different solvents ((a) in ACN,
113 (b) in water) observed by the PI-PM method. The irradiated region by the pump light corresponds to
114 the brighter regions in the images. The contrast of images originated from the refractive index change
115 due to photo-excited charge carriers in these regions. Although the images in ACN retained overall
116 brightness until 10-100 μ s, the bright regions in water gradually faded out for 1 μ s. The overall
117 refractive index change decayed due to the charge recombination; however, images in ACN did not
118 show a simple single-component decay. Furthermore, it was noticed that the brightness in the excited
119 regions in images strongly depended on the sample position, meaning that the materials in this sample

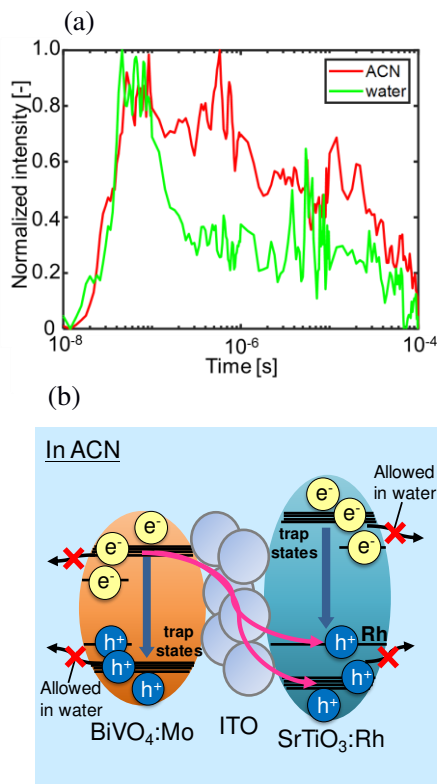
120 were not homogeneously distributed on the substrate.



121 Fig.1 The image sequence of the refractive index change after photo-excitation by a UV pump
122 light for SrTiO₃:Rh/ITO/BiVO₄:Mo (STOR/ITO/BVOM) Z-scheme water splitting sheet measured by
123 the patterned-illumination time-resolved phase microscope (PI-PM) in different solvents ((a) in ACN,
124 (b) in water). (c) The light intensity pattern of the pump light and the selected regions for the cluster
125 analysis is indicated in red squares. The result of the cluster analysis for area No.1 is shown in Fig.5-
126 7, and the others are presented in Fig.S4-S8 in Supporting information (SI).

127

128 For the assignment of the response on the STOR/ITO/BVOM photocatalyst sheet in the two
129 different solutions, the temporal changes of the average contrast change of the refractive index images
130 were obtained, which were calculated by taking the Fourier amplitude of the periodic stripe pattern at
131 the spatial frequency corresponding to the inverse of the stripe spacing, and it is shown in Fig.2(a).
132 The detailed calculation process was written in the previous papers.^{41,42} The signal response for the
133 STOR/ITO/BVOM in ACN were categorized into three response components; rapidly increased for
134 30 ns and decayed for 100 ns (first response), an additional rising for 1 μs and decayed for a couple
135 of μs (second response), a plateau until 10 μs and decay for 100 μs (third response).



137 Fig.2 (a) The average refractive index change response of STOR/ITO/BVOM until 100 μ s in
 138 acetonitrile (ACN) and water obtained from the PI-PM image sequence (Fig.1). The response was
 139 obtained from the signal amplitude at the light irradiated regions. (b) A schematic drawing of the
 140 charge transfer/decay processes for STOR/ITO/BVOM in ACN. Surface trapped carriers cannot be
 141 transferred to the solution side in ACN, where all the processes of charge dynamics are completed in
 142 the system.

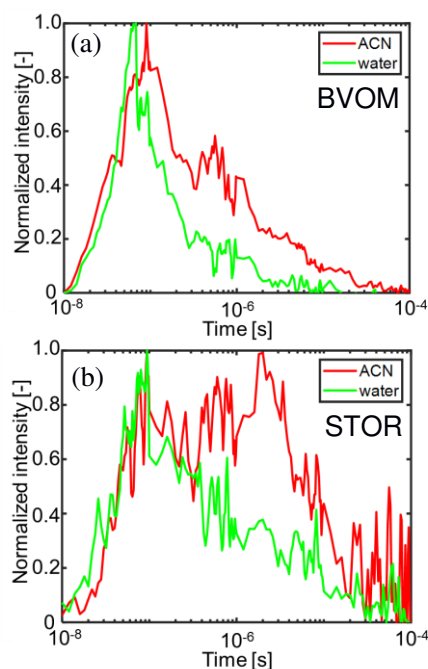
143

144 As shown in Fig. 2(b), photo-excited charge carriers were generated in the conduction band and
 145 valence band after the excitation because the wavelength of the pump laser was 355 nm, and its energy
 146 exceeds the bandgap energy of both materials (BiVO₄=2.4 eV, SrTiO₃=3.2 eV). Therefore, we
 147 monitored the charge carrier dynamics after the interband transition of both materials. These charge
 148 carriers were rapidly trapped to shallow or deep trap states originated from multiple types of defect.
 149 This trapping process almost finishes within the picosecond time region.^{21,22,44,45} These trapped charge
 150 carriers decayed due to the recombination inside the materials or the extraction outside the materials.
 151 The first component can be considered as the mixture of these fast charge carrier dynamics. Since
 152 ACN is an inert solvent for charge carriers, they were confined inside the materials. Thus, these
 153 carriers remained in a slower time scale, and the response was observed until hundreds of
 154 microseconds, which corresponds to the microsecond recombination for BiVO₄ and SrTiO₃,^{16,25}

155 included in the third component.

156 On the other hand, the second component in ACN disappeared in the water. It indicates that the
157 second component (100 ns to 1 μ s) in ACN was attributed to electrons in STOR or holes in BVOM
158 on the surfaces because these surface trapped charge carriers were consumed by water and utilized for
159 water splitting reactions. The loss of the component by water indicates that the corresponding charge
160 carriers were used for the water-splitting reactions, which are ensured by the fact that this
161 photocatalytic sheet had a high water splitting efficiency even for pure water (Fig. S11 in SI). Vice
162 versa, this result demonstrated that the surface trapped carriers were effectively extracted to water in
163 this system.

164 In terms of the Z-scheme water splitting system, the working mechanism is complicated, and
165 many processes of photo-excited charge carriers are included in the response. To simplify the
166 assignment, we investigated the charge carrier dynamics of BVOM and STOR separately, using the
167 same materials used for the Z-scheme system. Figure 3 shows the refractive index responses obtained
168 for BVOM and STOR in ACN and water, respectively. We could confirm the second components
169 (100 ns to 1 μ s) were observed in ACN in both samples, and they disappeared in water in both cases.
170 These results supported that these second components were attributed to the holes in BVOM and
171 electrons in STOR, respectively, and they were utilized for water splitting reactions, as shown in
172 Fig.2(b). It is supposed that the holes in BVOM and electrons in STOR for water splitting were
173 observed as a mixture in the response of the Z-scheme sample because these lifetimes matched by
174 chance. In addition to this finding, we could recognize that the second rising component was delayed
175 until 10 μ s in STOR in ACN. STOR has a mid-gap state corresponding to the $\text{Rh}^{3+/4+}$ state within the
176 bandgap. Rh is doped for the visible light absorption via the transition from the Rh^{3+} state to the
177 conduction band and the valence band to the Rh^{4+} state, corresponding to 2.3 and 2.7 eV,
178 respectively.^{18,46} The considerable delay of the response in STOR implies that the response of STOR
179 in ACN included unique components of photo-excited charge carriers due to the loss of the water-
180 splitting reactions in ACN instead of water.
181



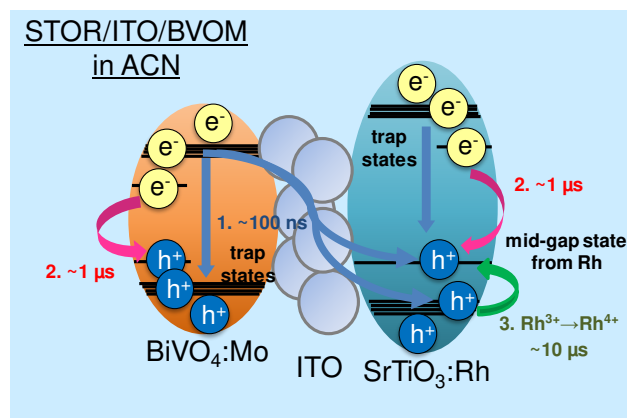
182 Fig.3 The average responses of the refractive index changes for (a) BVOM and (b) STOR until
 183 100 μ s in ACN and water obtained by the PI-PM image sequences.

184

185 A general understanding of the mechanism of the Z-scheme system is explained here, based on
 186 the description provided by Osterloh, et al.⁴⁷ By irradiation of the visible light, both BVOM and STOR
 187 are photo-excited, and the photo-generated holes in BVOM and photo-generated electrons in STOR
 188 are used for the water splitting to oxygen and hydrogen, respectively. Photo-excited electrons in
 189 BVOM are transferred to the neighboring STOR particles, and the Rh^{4+} elements are reduced to Rh^{3+}
 190 by the electron transfer. The Rh^{4+} elements work as the electron acceptor in this case. With regard to
 191 STOR, electrons are excited from the Rh^{3+} state to the conduction band for the visible light absorption,
 192 causing Rh^{4+} species generation. Water splitting continues when these reactions and charge transfer
 193 cycles repeatedly occur. It was reported that the Rh^{4+} states reduce the activity of water splitting by
 194 working as the recombination sites for the electrons in the conduction band, and much effort has been
 195 made to reduce the Rh^{4+} states.^{18,46} In our experiments, it was confirmed that the slow rising until 10
 196 μ s in STOR in ACN was due to the formation of the Rh^{4+} state by the hole transfer from the valence
 197 band to the Rh^{3+} states, as understood from the experiment of the methanol (MeOH) scavenger effect,
 198 as described in detail in Fig. S1 in Supporting Information (SI).

199 The schematic flow of the whole charge dynamics of STOR/ITO/BVOM is summarized in Fig.4.
 200 Based on the series of results, we concluded the response included at least three components. As a first
 201 step, photo-excited charge carriers decayed for <100 ns due to the intrinsic recombination processes
 202 because the responses in this time region were not influenced by water. During these processes, free
 203 charge carriers and trapped charge carriers at shallow trap states recombined inside each material.

204 (first component) The processes could include the recombination between the electrons in BVOM and
 205 the holes in STOR as well because of the smooth charge transfer via the ITO binder. In the second
 206 component, until $\sim 1 \mu\text{s}$, the response decayed due to the recombination of the surface-trapped charge
 207 carriers in ACN. The components were lost for water splitting when the photocatalytic sheets had
 208 contact with water. This response includes the contributions from both of the electrons in STOR and
 209 the holes in BVOM, considering the responses of STOR and BVOM only (Fig.3). The third component
 210 until $\sim 100 \mu\text{s}$ includes the hole accumulation decayed process from the valence band to Rh^{3+} state in
 211 STOR ($\sim 10 \mu\text{s}$) because this component was observed for STOR only and was quenched well by
 212 MeOH. The third component also includes other slower recombination processes. The hole
 213 accumulation in STOR contributed less in the Z-scheme system because ITO worked to mediate the
 214 electron transfer in BVOM to STOR and effectively reduce the Rh^{4+} state. However, we could confirm
 215 the accumulation of Rh^{4+} (slow rising component) was enhanced due to inefficient electron transfer
 216 from BVOM without the charge transfer mediator (ITO binder) (Refer to Section of 'The effect of
 217 ITO binder' and Fig.S2 and S3, for the detailed discussion on the ITO binder). In terms of the water
 218 splitting, the effective charges on each material in the second process are essential, and the high
 219 efficiency of water splitting of this Z-scheme system is possibly due to the well-matching of the
 220 lifetimes of the surface-trapped electrons in STOR and holes in BVOM. Furthermore, the oxidized
 221 Rh^{4+} state was reduced effectively by the smooth electron transfer from BVOM; otherwise, the state
 222 is well-known to deteriorate the hydrogen-generating electrons in STOR due to the recombination.
 223

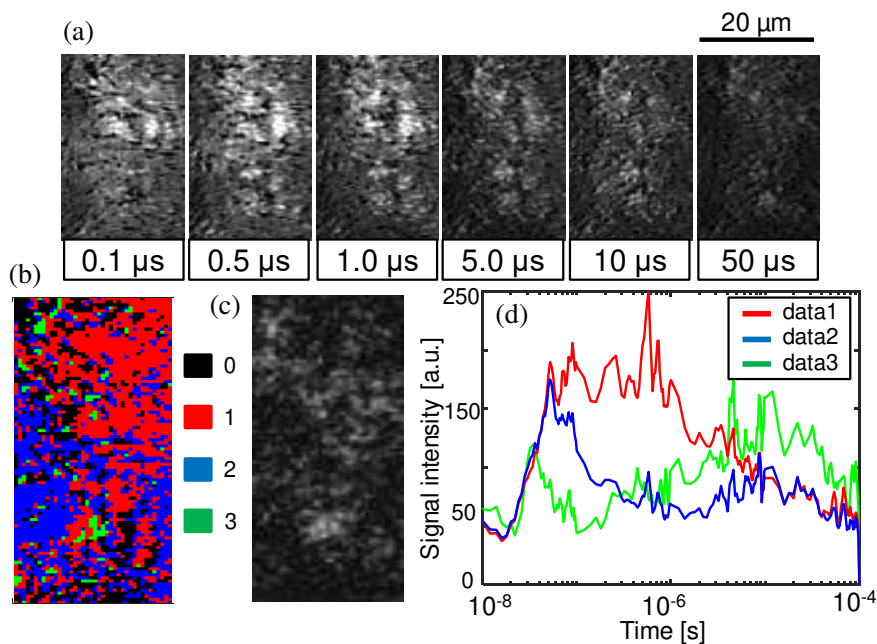


224 Fig.4 The schematic flow diagram of the whole charge dynamics in STOR/ITO/BVOM in ACN.
 225 Step 1 includes intrinsic recombination inside materials and charge transfer between two materials.
 226 Step 2 indicates the decay of surface trapped charge carriers in ACN, which are utilized for water
 227 splitting reactions with water outside. Step 3 includes the hole trapping to $\text{Rh}^{3+}/4+$ state in STOR and
 228 the slower recombination.

229

230 Many types of charge carrier responses were overlapped for the Z-scheme systems because they

231 consisted of more than one material. Furthermore, we noticed the inhomogeneity of the responses in
 232 the image sequences measured by the PI-PM method. Hence, we categorized the position-dependent
 233 (local) responses based on their similarity by the clustering analysis of the transient image sequence.
 234 A detailed procedure of this analysis was introduced in our previous paper.⁴³ Briefly, one of the local
 235 regions in the excited area was selected for the analysis, and the local responses in the selected region
 236 were extracted from each pixel in the image sequence. These responses were classified into several
 237 categories of the charge carrier responses based on the similarity calculated by the rise and decay
 238 profile. We applied this analysis to the local responses in the image sequence of STOR/ITO/BVOM
 239 in ACN (Fig.5). The selected position for the analysis is indicated in the red square in Fig.1(c) (No.1).
 240 Figure 5(a) shows a sequence of the temporal images of the refractive index change, representing a
 241 position-dependent response, where some micron-sized particles showed a large refractive index
 242 change with higher brightness, lasting until 1 μs , and fading out for 10 μs .
 243



244 Fig.5 (a) An image sequence of the refractive index change for STOR/ITO/BVOM in ACN in a
 245 square region ($20 \times 50 \mu\text{m}$) corresponding to No.1 in Fig.1(c) on the order from nanoseconds to
 246 microseconds. The scale bar corresponds to 20 μm . (b) The categorized mapping of the charge carrier
 247 responses of (a). An outlier positioned far from all categories were colored in black (#0). (c) A
 248 microscopic image in the same area as (a). (d) The averaged responses for each category in (b) are
 249 shown.

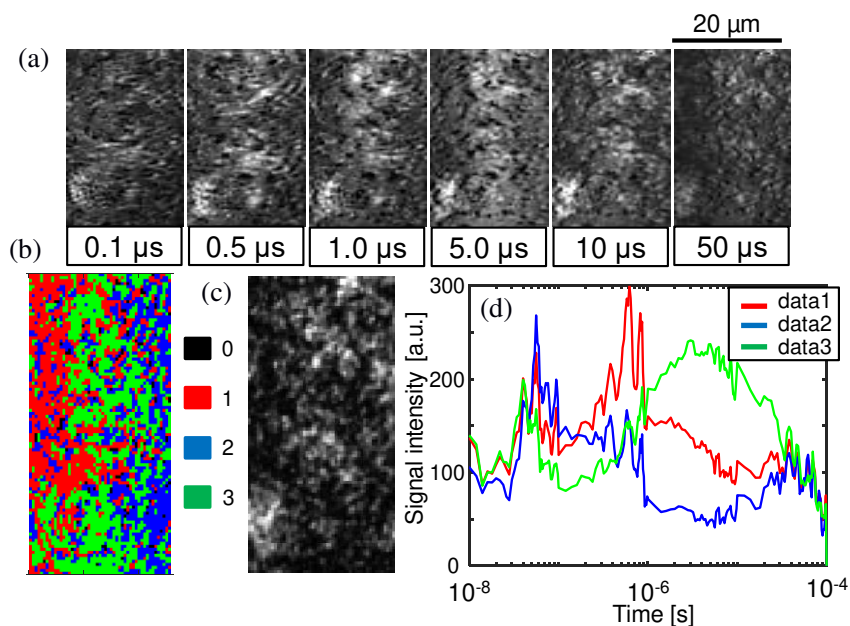
250

251 From the spectral clustering,⁴⁸ the transient responses were classified into three categories,
 252 and they were mapped out in Fig.5(b). The outliers, far from the three categories, were indicated as #0

253 (black) in this mapping. The original microscopic phase image of the sample is shown in Fig. 5(c). In
254 the sample image, aggregations with a few microns in diameter were recognized. The bright positions
255 in the transient image sequence were almost overlapped with the positions of the aggregations. In each
256 category, the responses at all the pixels in the same category were averaged and shown in Fig.5(d).
257 From Fig.5(b) and (d), the categorized map was mostly composed of red and blue regions. Based on
258 the assignment in Fig.2(a), the response in the red region was similar to an averaged overall response
259 (data1 in (d)), and the blue response seems to be composed of the first and third responses (data2 in
260 (d)). There was a small portion of green regions in Fig.5(b), and it showed a slow rising component
261 corresponding to the third component (data3 in (d)). Based on the assignment described earlier, the
262 response of data1 in Fig.5(d) was composed of the intrinsic recombination and the decay of the surface
263 trapped carriers until 1 μ s utilized for water splitting reactions. Therefore, water splitting reactions
264 should mostly occur in the red region. The blue response was composed of the intrinsic recombination
265 with the hole decay to Rh³⁺ state (Rh⁴⁺ formation) in STOR. The area of the green regions,
266 corresponding to Rh⁴⁺ formation in Fig.5(d), was much smaller compared with the red and blue regions.
267 It means that the blue and green regions do not have a water-splitting activity. This analysis was
268 applied to other regions (No.2~No.4 in Fig.1(c)), and the results are shown in Fig.S4-S6 in SI. Figure
269 S4 and S5 had almost the same categories of the responses as Fig.5. However, the red regions mostly
270 occupied the whole area compared with Fig.5. It means that regions No.2 and No.3 were more active
271 for water splitting reactions than that for region No.1. On the other hand, as shown in Fig.S6, the
272 green region increased for region No.4. It indicated the Rh⁴⁺ formation process was observed in a large
273 portion of this region, leading to ineffective water-splitting. Based on these results, each material was
274 not dispersed homogeneously and mixed well on the substrate, indicating that some regions were not
275 an ideal STOR/ITO/BVOM composition.

276 The same analysis was conducted in the case of a Z-scheme sample without the ITO binder
277 (STOR/BVOM) to confirm the effect of ITO (Fig.6). As you can see from these results, the same types
278 of categories for transient responses were found. However, the area of the green regions in the
279 categorized map (Fig.6(b)) drastically increased, while the number of the red region decreased
280 considerably compared with Fig.5(b). The ratio of the blue region remained almost the same. This
281 result indicated that the area of the Rh⁴⁺ formation drastically increased if there was no ITO binder in
282 the system. This is exactly the reason why the water splitting reaction was inefficient for this system.
283 Additionally, the green region was observed at the positions of aggregations in the sample image
284 (Fig.5(c)). It implies that the recognized aggregation in the sample image corresponded to the positions
285 of the STOR particle aggregates. The same experiments and analyses were applied to other regions
286 (No.2 and No.3 in Fig.1 (c)), and the results are shown in Fig.S7 and S8. We could confirm that the
287 Rh⁴⁺ formation occurred in a large portion of these regions. From the combination of the transient
288 image sequence and the spectral clustering, we could successfully visualize the position where the

289 water-splitting reactions proceeded and clarify the role of ITO for higher efficiency. Since the
 290 positions for the high and low efficiencies of water splitting reactions were spatially separated, it
 291 indicates that the charge transfer between BVOM and STOR were efficient in some regions and not
 292 in other regions, and possibly can be improved by the mixing and deposition conditions on the
 293 substrate.

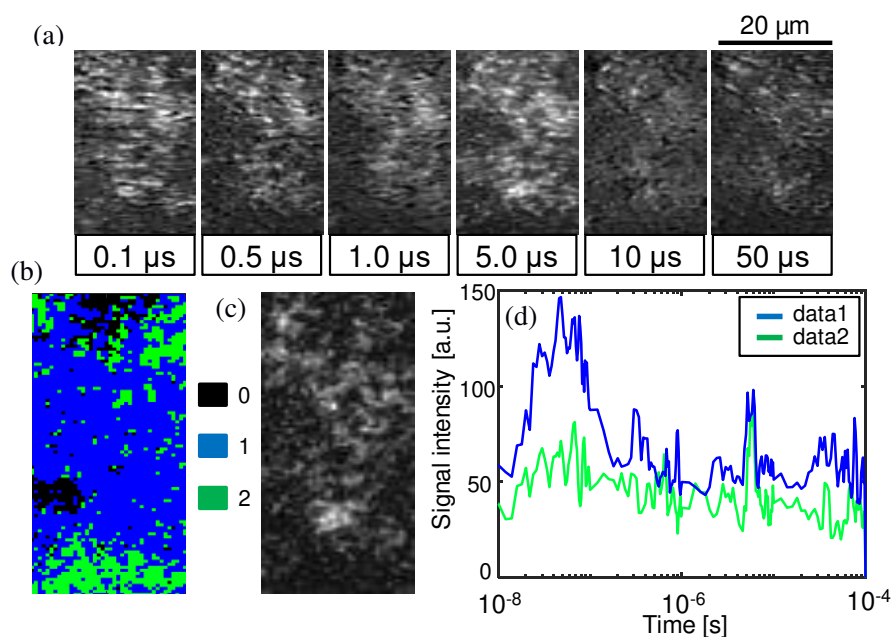


294 Fig.6 (a) An image sequence of the refractive index response for STOR/BVOM in ACN in a
 295 square region ($18 \times 50 \mu\text{m}$) corresponding to No.1 in Fig.1(c) on the order from nanoseconds to
 296 microseconds. The scale bar corresponds to $20 \mu\text{m}$. (b) The categorized mapping of the charge carrier
 297 responses of (a). An outlier positioned far from all categories were colored in black (#0). (c) A
 298 microscopic image in the same area as (a). (d) The averaged responses for each category in (b) are
 299 shown.

300

301 Finally, we studied that the local responses of STOR/ITO/BVOM in water by using the same
 302 cluster analysis to compare the difference from the results in ACN, as shown in Fig.7. The analysis
 303 was applied for the exactly same region as the region in Fig.5, and only the solvent was replaced with
 304 water. From Fig.7 (b) and (d), the categorized map was composed of the blue and green regions,
 305 corresponding to the fast decay (data1) and the weak response (data2) regions, and we could not
 306 observe the red and green regions found under the ACN condition (Fig.5). This result indicated that
 307 all the surface trapped charge carriers in the case of ACN were utilized for water splitting reactions in
 308 water. These components were completely removed by water, and only intrinsic recombination was
 309 observed. The comparison of the results in Fig.5 and 7 ensures the reaction of water splitting on the
 310 surface.

311 The categorization of local charge carrier responses with a combination of the PI-PM
 312 measurements and the clustering analyses reported herein provides useful information for designing
 313 and fabricating highly-efficient photocatalytic films or devices that have heterojunctions between
 314 different semiconductor particles. This method can positively affect a broad range of physicochemical
 315 processes that involve solid-state electron transfer.
 316
 317



318 Fig.7 (a) An image sequence of the refractive index response for STOR/ITO/BVOM in water in
 319 a square region ($20 \times 50 \mu\text{m}$) corresponding to No.1 on the order from nanoseconds to microseconds.
 320 The location of the sample was exactly the same as Fig.5(a). The scale bar corresponds to 20 μm . (b)
 321 The categorized mapping of the charge carrier responses of (a). An outlier positioned far from all
 322 categories was colored in black (#0) (c) A microscopic image in the same area as (a). (d) The averaged
 323 responses for each category in (b) are shown.

324

325 Conclusion

326 This work revealed the origin of the efficient water splitting reactions in STOR/ITO/BVOM
 327 photocatalyst sheets that can split water to H_2 and O_2 under visible light by employing our original
 328 clustering analysis of photo-generated charge carrier responses in the transient image sequence. The
 329 combination of the observation technique (PI-PM) and the clustering analysis could lead to visualize
 330 reactive sites for efficient water-splitting reactions and inactive sites deteriorating water splitting

331 efficiency. From the averaged responses of the refractive index change for different combinations of
332 materials in various solvents, we could find three components, corresponding to the intrinsic
333 recombination of photo-excited charge carriers inside materials (~100 ns), recombination of surface
334 trapped charge carriers which can essentially contribute to split water (~1 μ s), and the hole trapping
335 (accumulation) to the Rh state in STOR, generating Rh⁴⁺ state (~10 μ s). Consequently, we could
336 visually demonstrate that the region of the hole trapping to the Rh state, where is the region to suppress
337 the water splitting reactions in the photocatalyst sheet, decreased in the sheet including ITO mediators
338 at the reaction sites due to the efficient inter-particle charge transfer. This technique will be a
339 powerful tool for the detection of active/inactive sites for the water-splitting materials but also the
340 other materials involving electron transfer reactions, providing swift optimization for photocatalytic
341 materials.

342

343 Method

344 The principle of the PI-PM is described in the previous papers.^{41,43} In brief, an arbitrary light
345 pattern is irradiated on a sample to excite charge carriers. The charge carriers decay or diffuse as time
346 passes due to the recombination, charge trapping, and transport, and the charge carrier distribution is
347 varied in time. The distribution of the photo-excited charge carriers is observed from the refractive
348 index change by the phase-sensitive imaging. The refractive index was imaged by the Talbot self-
349 imaging technique.⁴⁹ The pattern-illumination is required for applying various image recovery
350 algorithms, as described in a different paper.⁴¹ In this study, only the background correction was
351 processed before the analyses to prevent the loss of small features in images. In this optical
352 configuration, the TA responses could also be included in the image, but the refractive index change
353 was the major contribution to the signal, which could be confirmed by optimizing the focus position
354 because the TA signal intensity does not depend on the focus position.

355 The experimental setup is fully described in Fig. S9 in SI. Briefly, the wavelengths of the
356 pump and probe pulse lights were 355 and 532 nm, respectively, with pulse widths of 5 ns. The pump
357 light was illuminated as a Ronchi ruling pattern similar to the transient grating (TG) technique, as we
358 reported previously to understand the refractive index change response easily as the amplitude change
359 by Fourier transform. The width of each line in the ruling-pattern was 25 μ m, and the spacing was 45
360 μ m.

361 The sample was Rh-doped SrTiO₃ and Mo-doped BiVO₄, including ITO nanoparticles as a
362 conductive binder, and printed on a glass substrate with a thickness of 1 μ m. The detailed preparation
363 method is described in SI. The SEM images of Rh-doped SrTiO₃ and Mo-doped BiVO₄ are shown in
364 Fig. S10 in SI. The average diameters of them were 300 nm and 2 μ m, respectively. The gas evolution
365 data for this photocatalyst sheet in pure water is shown in Fig. S11 in SI, and the STH was 0.4 %.

366 The solid/liquid interface was prepared by putting another glass slide together with a silicon
367 rubber spacer (thickness: 0.5 mm), and liquids were sandwiched within the gap. Each film sample was
368 measured in contact with acetonitrile (ACN) and water. ACN is an inert solvent for photocatalytic
369 reactions, where no charge transfer at the interface is guaranteed,²⁸ while it occurs for water. We used
370 methanol (MeOH) as a hole scavenger for assignment and confirmation of the hole responses.

371

372 **Supporting Information**

373 Fig. S1 The transient responses of STOM for the scavenger.

374 Fig. S2 The transient responses of Z-scheme sample with and without ITO.

375 Fig. S3 The transient responses of Z-scheme sample without ITO for the scavenger.

376 Fig. S4 Mapping example of the charge responses for Z-scheme sample in region No.2.

377 Fig. S5 Mapping example of the charge responses for Z-scheme sample in region No.3.

378 Fig. S6 Mapping example of the charge responses for Z-scheme sample in region No.4.

379 Fig. S7 Mapping example of the charge responses for Z-scheme sample without ITO in region
380 No.2.

381 Fig. S8 Mapping example of the charge responses for Z-scheme sample without ITO in region
382 No.3.

383 Fig. S9 Experimental setup of PI-PM method.

384 Fig. S10 SEM images of STOR and BVOM.

385 Fig. S11 Oxygen and hydrogen evolution experiment for Z-scheme sample.

386

387

388 **Author Contribution Statement**

389 ME, HT and KK designed the experiments and made measurements. TI, SO, HT, and KD prepared
390 the photocatalytic sheet. ME analyzed the data, and ME, HT, KD, and KK considered the result. ME
391 and KK wrote the manuscript, and all the authors reviewed it.

392

393 **Declaration of competing interests**

394 I declare that the authors have no competing interests or other interests that might be
395 perceived to influence the results and/or discussion reported in this article.

396

397 **Acknowledgments**

398 The research was financially supported by JST PRESTO (#JPMJPR1675), and the Institute of Science
399 and Engineering, Chuo University.

400

401 References

- 402 1. Wang, Z., Li, C. & Domen, K. Recent developments in heterogeneous photocatalysts for solar-
403 driven overall water splitting. *Chem. Soc. Rev.* **48**, 2109–2125 (2019).
- 404 2. Wang, Q. & Domen, K. Particulate Photocatalysts for Light-Driven Water Splitting: Mechanisms,
405 Challenges, and Design Strategies. *Chem. Rev.* **120**, 919–985 (2020).
- 406 3. Djurišić, A. B., He, Y. & Ng, A. M. C. Visible-light photocatalysts: Prospects and challenges.
407 *APL Mater.* **8**, 030903 (2020).
- 408 4. Hisatomi, T. & Domen, K. Reaction systems for solar hydrogen production via water splitting
409 with particulate semiconductor photocatalysts. *Nat. Catal.* **2**, 387–399 (2019).
- 410 5. Goto, Y. *et al.* A Particulate Photocatalyst Water-Splitting Panel for Large-Scale Solar Hydrogen
411 Generation. *Joule* **2**, 509–520 (2018).
- 412 6. Takata, T. *et al.* Photocatalytic water splitting with a quantum efficiency of almost unity. *Nature*
413 **581**, 411–414 (2020).
- 414 7. Zhao, Z. *et al.* Electronic structure basis for enhanced overall water splitting photocatalysis with
415 aluminum doped SrTiO₃ in natural sunlight. *Energy Environ. Sci.* **12**, 1385–1395 (2019).
- 416 8. Maeda, K. Z-Scheme Water Splitting Using Two Different Semiconductor Photocatalysts. *ACS*
417 *Catal.* **3**, 1486–1503 (2013).
- 418 9. Abe, R., Sayama, K., Domen, K. & Arakawa, H. A new type of water splitting system composed

- 419 of two different TiO₂ photocatalysts (anatase, rutile) and a IO₃⁻/I⁻ shuttle redox mediator. *Chem.*
420 *Phys. Lett.* **344**, 339–344 (2001).
- 421 10. Ng, B.-J. *et al.* Z-Scheme Photocatalytic Systems for Solar Water Splitting. *Adv. Sci.* **7**, 1903171
422 (2020).
- 423 11. Full Text PDF.
- 424 12. Wang, Q. *et al.* Z-scheme water splitting using particulate semiconductors immobilized onto
425 metal layers for efficient electron relay. *J. Catal.* **328**, 308–315 (2015).
- 426 13. Wang, Q. *et al.* Scalable water splitting on particulate photocatalyst sheets with a solar-to-
427 hydrogen energy conversion efficiency exceeding 1%. *Nat. Mater.* **15**, 611–615 (2016).
- 428 14. Wang, Q. *et al.* Printable Photocatalyst Sheets Incorporating a Transparent Conductive Mediator
429 for Z-Scheme Water Splitting. *Joule* **2**, 2667–2680 (2018).
- 430 15. Okunaka, S. *et al.* Z-Scheme Water Splitting under Near-Ambient Pressure using a Zirconium
431 Oxide Coating on Printable Photocatalyst Sheets. *ChemSusChem* **13**, 4906–4910 (2020).
- 432 16. Yamakata, A., Kawaguchi, M., Murachi, R., Okawa, M. & Kamiya, I. Dynamics of
433 Photogenerated Charge Carriers on Ni- and Ta-Doped SrTiO₃ Photocatalysts Studied by Time-
434 Resolved Absorption and Emission Spectroscopy. *J. Phys. Chem. C* **120**, 7997–8004 (2016).
- 435 17. Ichihara, F. *et al.* Photogenerated Charge Carriers Dynamics on La- and/or Cr-Doped SrTiO₃
436 Nanoparticles Studied by Transient Absorption Spectroscopy. *J. Phys. Chem. C* **124**, 1292–1302

- 437 (2020).
- 438 18. Furuhashi, K., Jia, Q., Kudo, A. & Onishi, H. Time-Resolved Infrared Absorption Study of
439 SrTiO₃ Photocatalysts Codoped with Rhodium and Antimony. *J. Phys. Chem. C* **117**, 19101–
440 19106 (2013).
- 441 19. Cooper, J. K. *et al.* Physical Origins of the Transient Absorption Spectra and Dynamics in Thin-
442 Film Semiconductors: The Case of BiVO₄. *J. Phys. Chem. C* **122**, 20642–20652 (2018).
- 443 20. Aiga, N. *et al.* Electron–Phonon Coupling Dynamics at Oxygen Evolution Sites of Visible-Light-
444 Driven Photocatalyst: Bismuth Vanadate. *J. Phys. Chem. C* **117**, 9881–9886 (2013).
- 445 21. Ravensbergen, J. *et al.* Unraveling the Carrier Dynamics of BiVO₄: A Femtosecond to
446 Microsecond Transient Absorption Study. *J. Phys. Chem. C* **118**, 27793–27800 (2014).
- 447 22. Suzuki, Y. *et al.* Rational Interpretation of Correlated Kinetics of Mobile and Trapped Charge
448 Carriers: Analysis of Ultrafast Carrier Dynamics in BiVO₄. *J. Phys. Chem. C* **121**, 19044–19052
449 (2017).
- 450 23. Selim, S. *et al.* Impact of Oxygen Vacancy Occupancy on Charge Carrier Dynamics in BiVO₄
451 Photoanodes. *J. Am. Chem. Soc.* **141**, 18791–18798 (2019).
- 452 24. Grigioni, I. *et al.* In Operando Photoelectrochemical Femtosecond Transient Absorption
453 Spectroscopy of WO₃/BiVO₄ Heterojunctions. *ACS Energy Lett.* **4**, 2213–2219 (2019).
- 454 25. Selim, S. *et al.* WO₃/BiVO₄: impact of charge separation at the timescale of water oxidation.

- 455 *Chem. Sci.* **10**, 2643–2652 (2019).
- 456 26. Katayama, K., Yamaguchi, M. & Sawada, T. Lens-free heterodyne detection for transient grating
457 experiments. *Appl. Phys. Lett.* **82**, 2775–2777 (2003).
- 458 27. Okuda, M. & Katayama, K. Selective detection of real and imaginary parts of refractive index
459 change in solutions induced by photoexcitation using near-field heterodyne transient grating
460 method. *Chem. Phys. Lett.* **443**, 158–162 (2007).
- 461 28. Kuwahara, S. & Katayama, K. Distinction of electron pathways at titanium oxide/liquid interfaces
462 in photocatalytic processes and co-catalyst effects. *Phys. Chem. Chem. Phys.* **18**, 25271–25276
463 (2016).
- 464 29. Kuwahara, S. *et al.* Detection of non-absorbing charge dynamics via refractive index change in
465 dye-sensitized solar cells. *Phys. Chem. Chem. Phys.* **15**, 5975–5981 (2013).
- 466 30. Shen, Q. *et al.* Photoexcited hole dynamics in TiO₂ nanocrystalline films characterized using a
467 lens-free heterodyne detection transient grating technique. *Chem. Phys. Lett.* **419**, 464–468 (2006).
- 468 31. Hata, H., Katayama, K., Shen, Q. & Toyoda, T. Characterization of Photoexcited Carriers and
469 Thermal Properties of Nanoparticulate TiO₂ Film Using Heterodyne Transient Grating Method.
470 *Jpn. J. Appl. Phys.* **51**, 42601 (2012).
- 471 32. Shingai, D., Ide, Y., Sohn, W. Y. & Katayama, K. Photoexcited charge carrier dynamics of
472 interconnected TiO₂ nanoparticles: evidence of enhancement of charge separation at anatase–

- 473 rutile particle interfaces. *Phys. Chem. Chem. Phys.* **20**, 3484–3489 (2018).
- 474 33. Inaba, M., Katayama, K. & Sohn, W. Y. Cooperative effects of surface and interface treatments
475 in a hematite (α -Fe₂O₃) photo-anode on its photo-electrochemical performance. *Sustain. Energy*
476 *Fuels* **4**, 2174–2183 (2020).
- 477 34. Sohn, W. Y. *et al.* Uncovering Photo-Excited Charge Carrier Dynamics in Hematite (α -Fe₂O₃)
478 Hidden in the Nanosecond Range by the Heterodyne Transient Grating Technique Combined with
479 the Randomly Interleaved Pulse-Train Method. *J. Phys. Chem. C* **123**, 6693–6700 (2019).
- 480 35. Sohn, W. Y. *et al.* Charge carrier kinetics in hematite with NiFeO_x coating in aqueous solutions:
481 Dependence on bias voltage. *J. Photochem. Photobiol. Chem.* **353**, 344–348 (2018).
- 482 36. Zhu, Y. & Cheng, J.-X. Transient absorption microscopy: Technological innovations and
483 applications in materials science and life science. *J. Chem. Phys.* **152**, 020901 (2020).
- 484 37. Simpson, M. J., Doughty, B., Yang, B., Xiao, K. & Ma, Y.-Z. Imaging Electronic Trap States in
485 Perovskite Thin Films with Combined Fluorescence and Femtosecond Transient Absorption
486 Microscopy. *J. Phys. Chem. Lett.* **7**, 1725–1731 (2016).
- 487 38. Gao, Y., Nie, W., Wang, X., Fan, F. & Li, C. Advanced space- and time-resolved techniques for
488 photocatalyst studies. *Chem. Commun.* **56**, 1007–1021 (2020).
- 489 39. Wang, L., Tahir, M., Chen, H. & Sambur, J. B. Probing Charge Carrier Transport and
490 Recombination Pathways in Monolayer MoS₂/WS₂ Heterojunction Photoelectrodes. *Nano Lett.*

- 491 **19**, 9084–9094 (2019).
- 492 40. Todt, M. A., Isenberg, A. E., Nanayakkara, S. U., Miller, E. M. & Sambur, J. B. Single-Nanoflake
493 Photo-Electrochemistry Reveals Champion and Spectator Flakes in Exfoliated MoSe₂ Films. *J.*
494 *Phys. Chem. C* **122**, 6539–6545 (2018).
- 495 41. Katayama, K. Photo-excited charge carrier imaging by time-resolved pattern illumination phase
496 microscopy. *J. Chem. Phys.* **153**, 054201 (2020).
- 497 42. Ebihara, M., Sohn, W. Y. & Katayama, K. Lifetime mapping of photo-excited charge carriers by
498 the transient grating imaging technique for nano-particulate semiconductor films. *Rev. Sci.*
499 *Instrum.* **90**, 073905 (2019).
- 500 43. Ebihara, M. & Katayama, K. Anomalous Charge Carrier Decay Spotted by Clustering of a Time-
501 Resolved Microscopic Phase Image Sequence. *J. Phys. Chem. C* **124**, 23551–23557 (2020).
- 502 44. Kato, K., Jiang, J., Sakata, Y. & Yamakata, A. Effect of Na-Doping on Electron Decay Kinetics
503 in SrTiO₃ Photocatalyst. *ChemCatChem* **11**, 6349–6354 (2019).
- 504 45. Kato, K. & Yamakata, A. Defect-Induced Acceleration and Deceleration of Photocarrier
505 Recombination in SrTiO₃ Powders. *J. Phys. Chem. C* **124**, 11057–11063 (2020).
- 506 46. Konta, R., Ishii, T., Kato, H. & Kudo, A. Photocatalytic Activities of Noble Metal Ion Doped
507 SrTiO₃ under Visible Light Irradiation. *J. Phys. Chem. B* **108**, 8992–8995 (2004).
- 508 47. Han, R., Melo, M. A., Zhao, Z., Wu, Z. & Osterloh, F. E. Light Intensity Dependence of

- 509 Photochemical Charge Separation in the BiVO₄/Ru-SrTiO₃:Rh Direct Contact Tandem
510 Photocatalyst for Overall Water Splitting. *J. Phys. Chem. C* **124**, 9724–9733 (2020).
- 511 48. von Luxburg, U. A tutorial on spectral clustering. *Stat. Comput.* **17**, 395–416 (2007).
- 512 49. Koehl, R. M., Adachi, S. & Nelson, K. A. Direct Visualization of Collective Wavepacket
513 Dynamics. *J. Phys. Chem. A* **103**, 10260–10267 (1999).
- 514

515 Figure captions

516

517 Fig.1 The image sequence of the refractive index change after photo-excitation by a UV pump light
518 for SrTiO₃:Rh/ITO/BiVO₄:Mo (STOR/ITO/BVOM) Z-scheme water splitting sheet measured by the
519 patterned-illumination time-resolved phase microscope (PI-PM) in different solvents ((a) in ACN, (b)
520 in water). (c) The light intensity pattern of the pump light and the selected regions for the cluster
521 analysis is indicated in red squares. The result of the cluster analysis for area No.1 is shown in Fig.5-
522 7, and the others are presented in Fig.S4-S8 in Supporting information (SI).

523

524 Fig.2 (a) The average refractive index change response of STOR/ITO/BVOM until 100 μs in
525 acetonitrile (ACN) and water obtained from the PI-PM image sequence (Fig.1). The response was
526 obtained from the signal amplitude at the light irradiated regions. (b) A schematic drawing of the
527 charge transfer/decay processes for STOR/ITO/BVOM in ACN. Surface trapped carriers cannot be
528 transferred to the solution side in ACN, where all the processes of charge dynamics are completed in
529 the system.

530

531 Fig.3 The average responses of the refractive index changes for (a) BVOM and (b) STOR until
532 100 μs in ACN and water obtained by the PI-PM image sequences.

533

534 Fig.4 The schematic flow diagram of the whole charge dynamics in STOR/ITO/BVOM in ACN.
535 Step 1 includes intrinsic recombination inside materials and charge transfer between two materials.
536 Step 2 indicates the decay of surface trapped charge carriers in ACN, which are utilized for water
537 splitting reactions with water outside. Step 3 includes the hole trapping to Rh^{3+/4+} state in STOR and
538 the slower recombination.

539

540 Fig.5 (a) An image sequence of the refractive index change for STOR/ITO/BVOM in ACN in a
541 square region (20×50 μm) corresponding to No.1 in Fig.1(c) on the order from nanoseconds to
542 microseconds. The scale bar corresponds to 20 μm. (b) The categorized mapping of the charge carrier
543 responses of (a). An outlier positioned far from all categories were colored in black (#0). (c) A
544 microscopic image in the same area as (a). (d) The averaged responses for each category in (b) are
545 shown.

546

547 Fig.6 (a) An image sequence of the refractive index response for STOR/BVOM in ACN in a
548 square region (18×50 μm) corresponding to No.1 in Fig.1(c) on the order from nanoseconds to
549 microseconds. The scale bar corresponds to 20 μm. (b) The categorized mapping of the charge carrier
550 responses of (a). An outlier positioned far from all categories were colored in black (#0). (c) A

551 microscopic image in the same area as (a). (d) The averaged responses for each category in (b) are
552 shown.

553

554 Fig.7 (a) An image sequence of the refractive index response for STOR/ITO/BVOM in water in
555 a square region ($20 \times 50 \mu\text{m}$) corresponding to No.1 on the order from nanoseconds to microseconds.

556 The location of the sample was exactly the same as the Fig.5(a). The scale bar corresponds to $20 \mu\text{m}$.

557 (b) The categorized mapping of the charge carrier responses of (a). An outlier positioned far from all

558 categories were colored in black (#0) (c) A microscopic image in the same area as (a). (d) The

559 averaged responses for each category in (b) are shown.

560

Figures

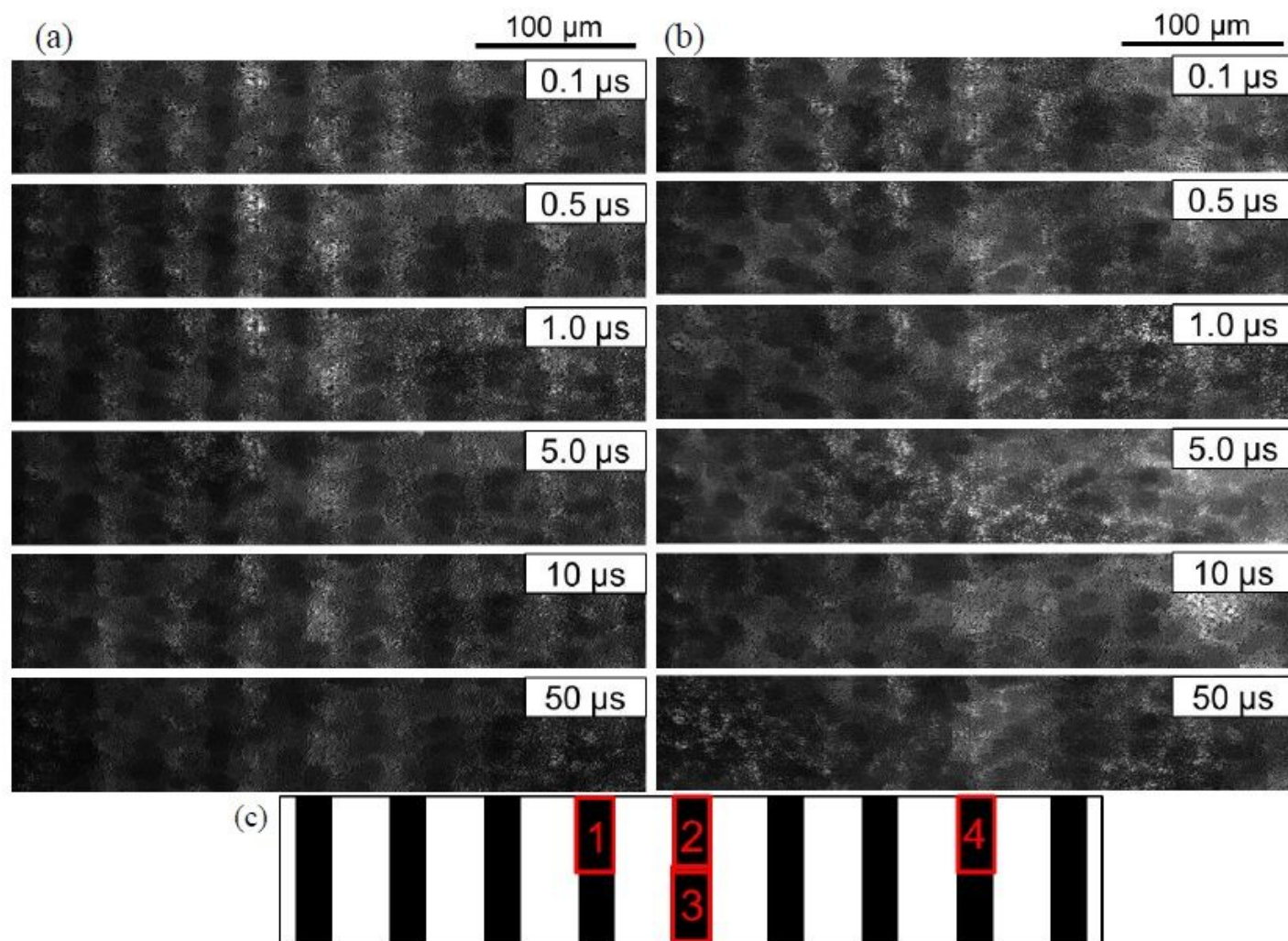


Figure 1

The image sequence of the refractive index change after photo-excitation by a UV pump light for SrTiO₃:Rh/ITO/BiVO₄:Mo (STOR/ITO/BVOM) Z-scheme water splitting sheet measured by the patterned-illumination time-resolved phase microscope (PI-PM) in different solvents ((a) in ACN, (b) in water). (c) The light intensity pattern of the pump light and the selected regions for the cluster analysis is indicated in red squares. The result of the cluster analysis for area No.1 is shown in Fig.5-7, and the others are presented in Fig.S4-S8 in Supporting information (SI)).

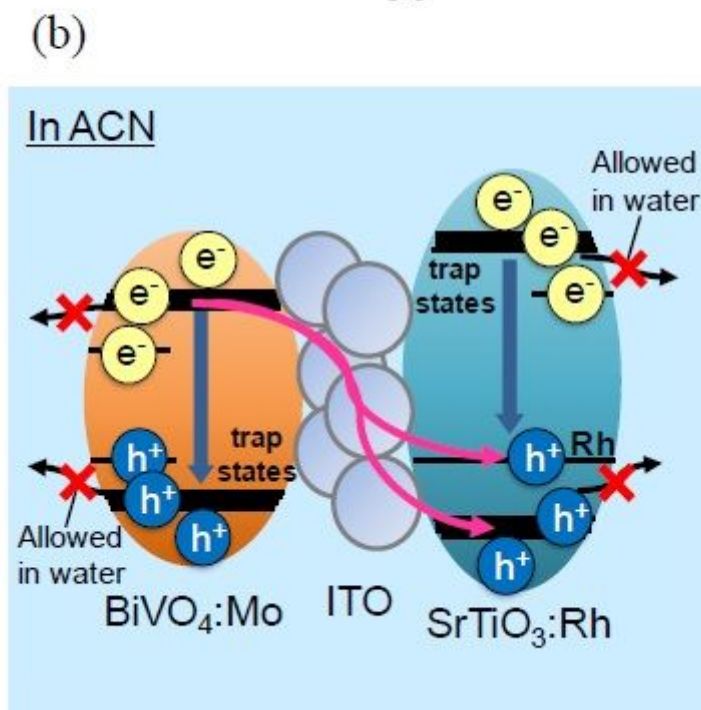
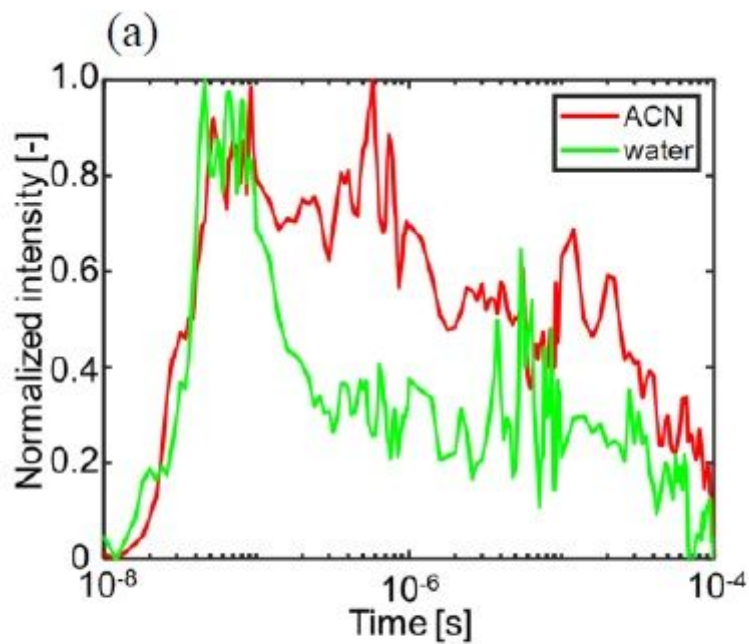


Figure 2

(a) The average refractive index change response of STOR/ITO/BVOM until 100 μ s in acetonitrile (ACN) and water obtained from the PI-PM image sequence (Fig.1). The response was obtained from the signal amplitude at the light irradiated regions. (b) A schematic drawing of the charge transfer/decay processes for STOR/ITO/BVOM in ACN. Surface trapped carriers cannot be transferred to the solution side in ACN, where all the processes of charge dynamics are completed in the system.

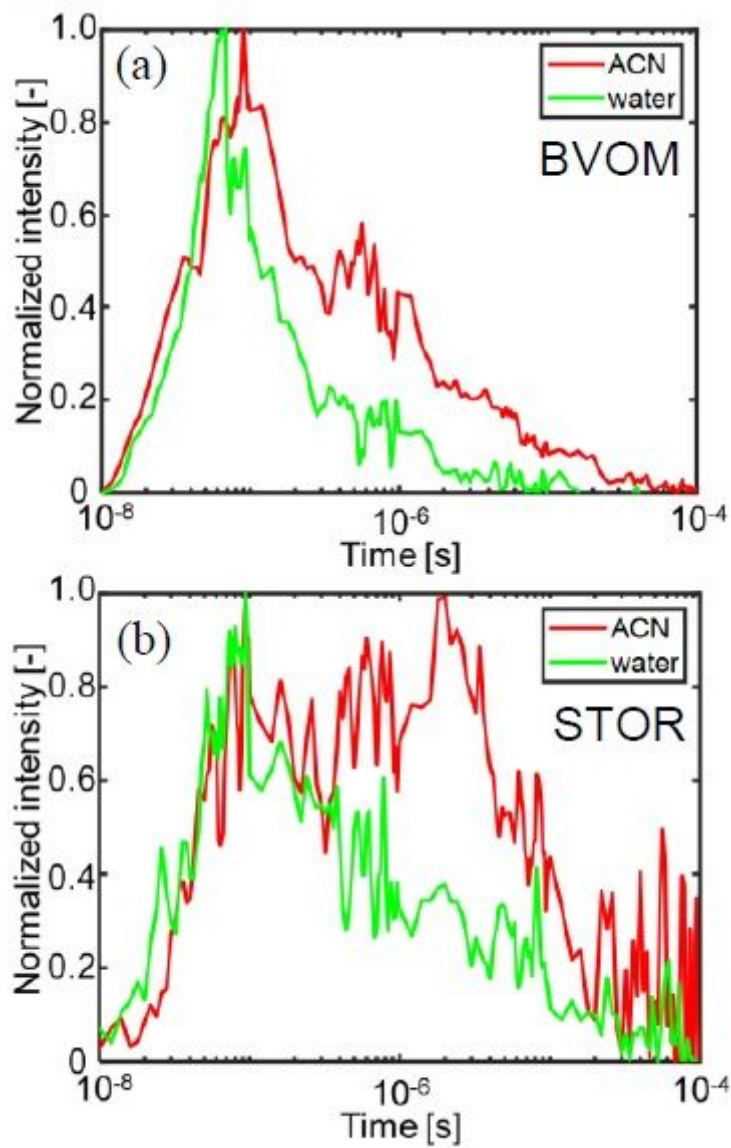


Figure 3

The average responses of the refractive index changes for (a) BVOM and (b) STOR until $100 \mu\text{s}$ in ACN and water obtained by the PI-PM image sequences.

STOR/ITO/BVOM in ACN

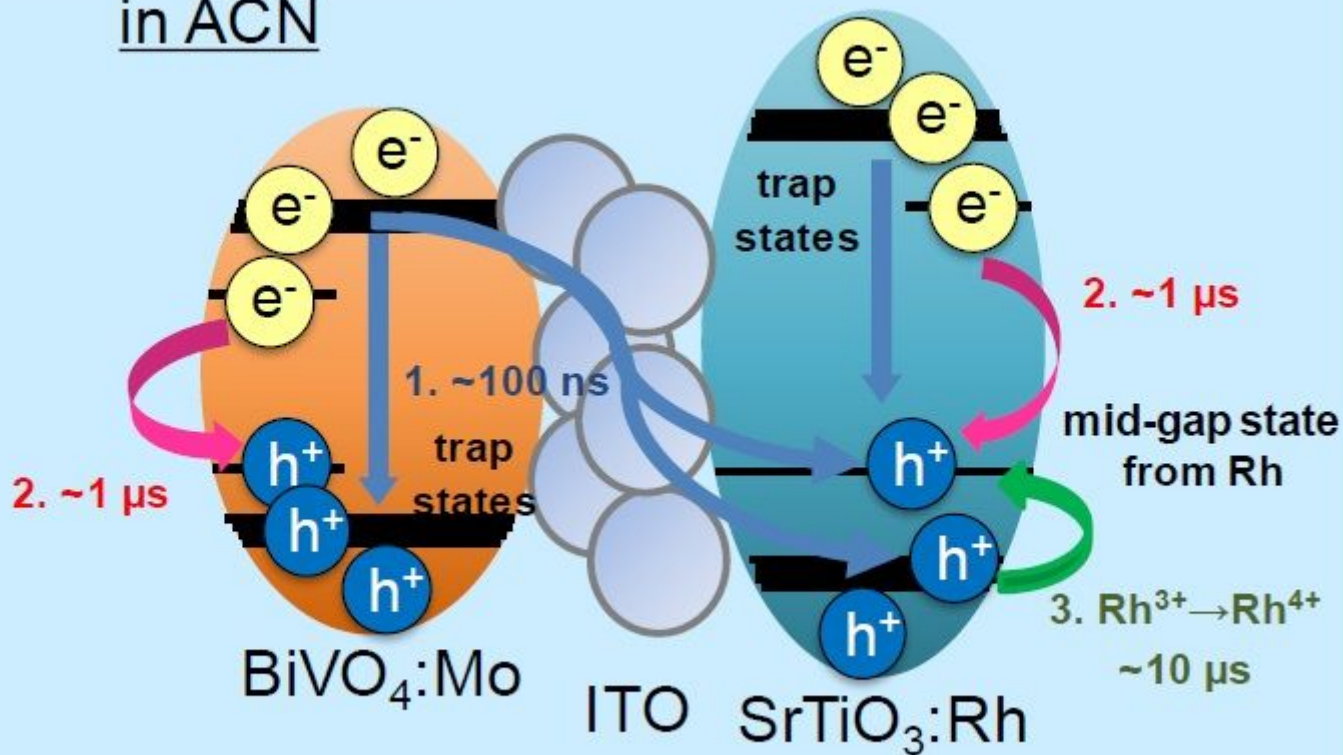


Figure 4

The schematic flow diagram of the whole charge dynamics in STOR/ITO/BVOM in ACN. Step 1 includes intrinsic recombination inside materials and charge transfer between two materials. Step 2 indicates the decay of surface trapped charge carriers in ACN, which are utilized for water splitting reactions with water outside. Step 3 includes the hole trapping to Rh³⁺/4⁺ state in STOR and the slower recombination.

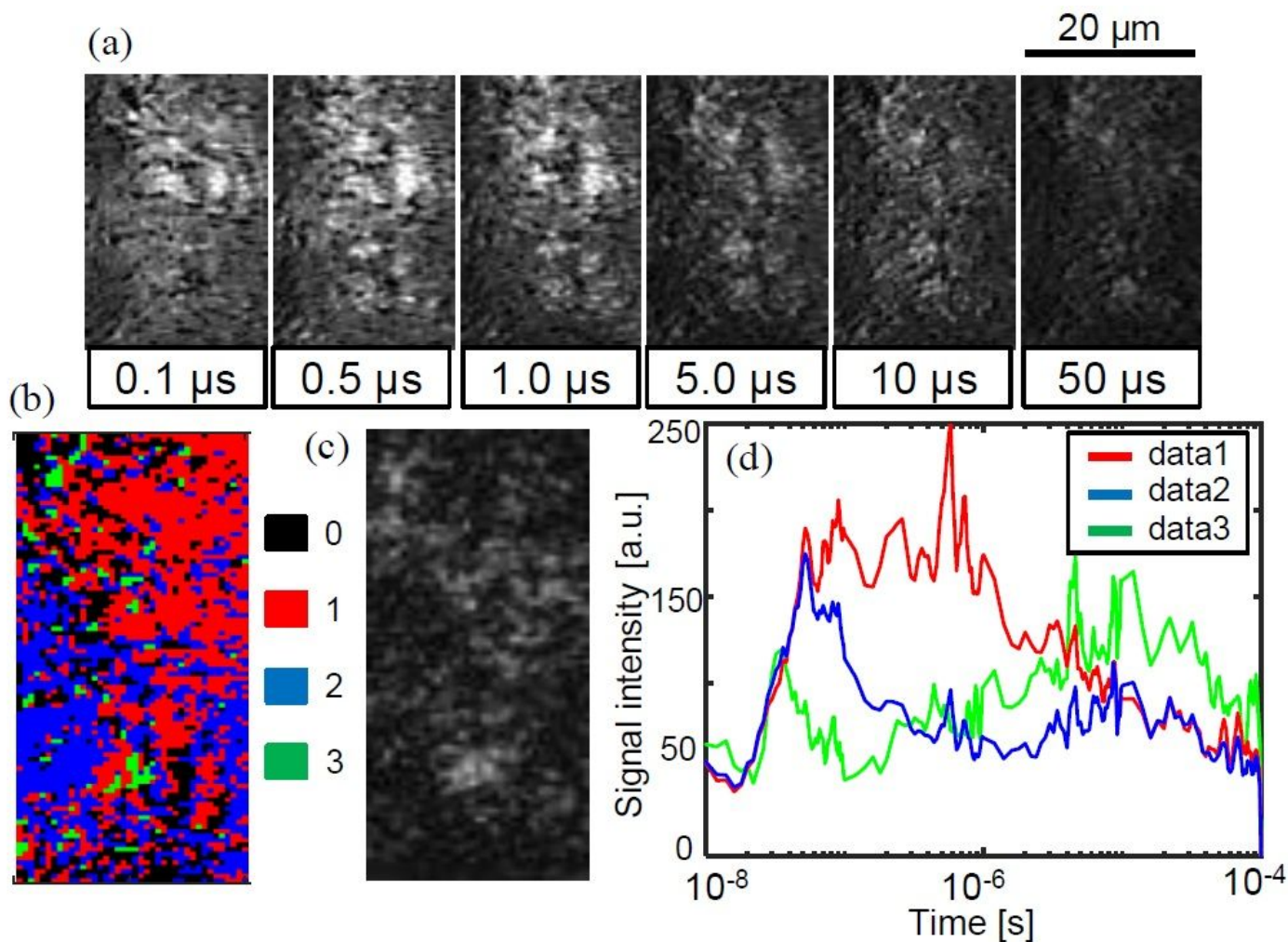


Figure 5

(a) An image sequence of the refractive index change for STOR/ITO/BVOM in ACN in a square region (20×50 μm) corresponding to No.1 in Fig.1(c) on the order from nanoseconds to microseconds. The scale bar corresponds to 20 μm. (b) The categorized mapping of the charge carrier responses of (a). An outlier positioned far from all categories were colored in black (#0). (c) A microscopic image in the same area as (a). (d) The averaged responses for each category in (b) are shown.

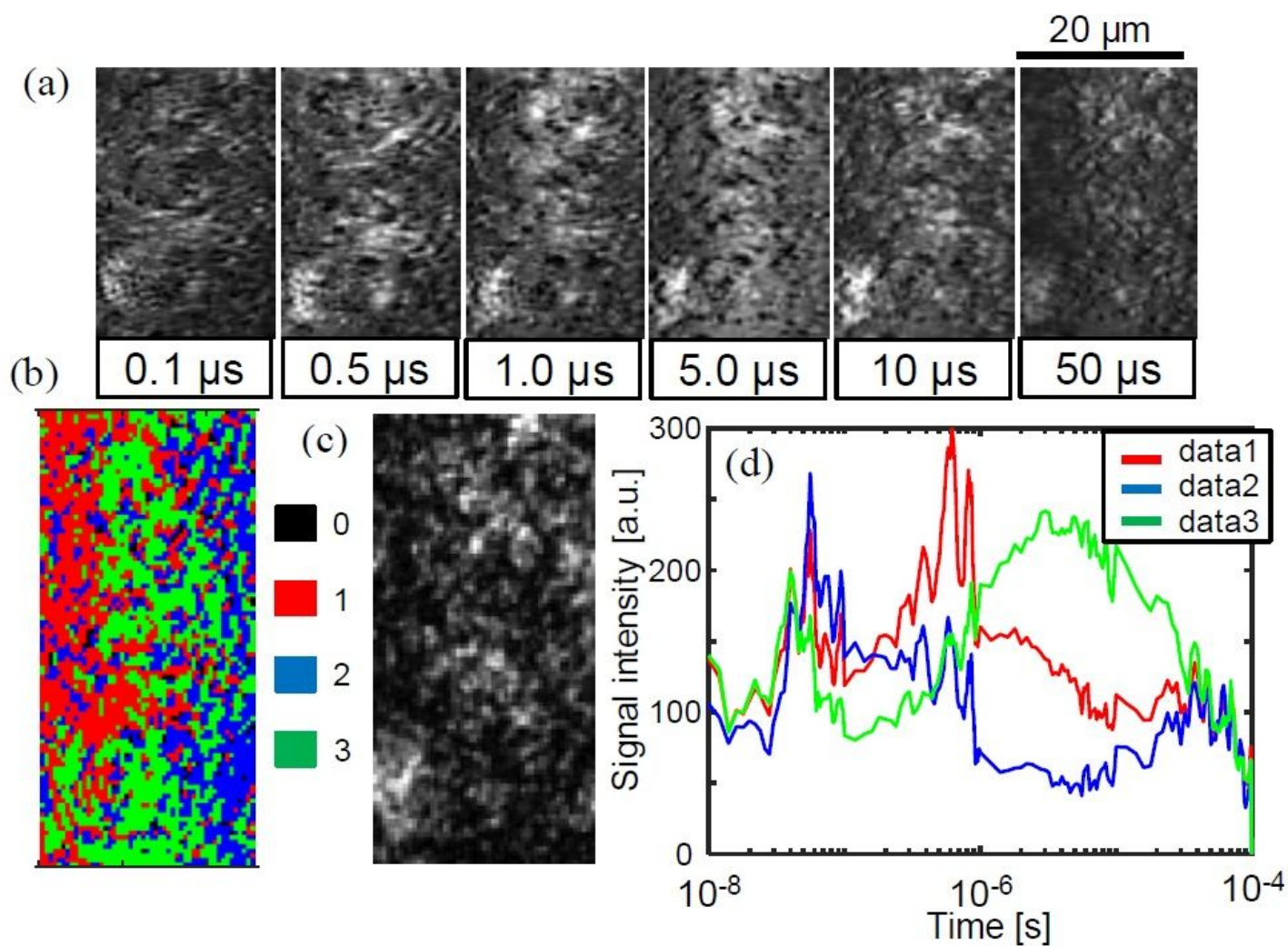


Figure 6

(a) An image sequence of the refractive index response for STOR/BVOM in ACN in a square region (18×50 μm) corresponding to No.1 in Fig.1(c) on the order from nanoseconds to microseconds. The scale bar corresponds to 20 μm. (b) The categorized mapping of the charge carrier responses of (a). An outlier positioned far from all categories were colored in black (#0). (c) A microscopic image in the same area as (a). (d) The averaged responses for each category in (b) are shown.

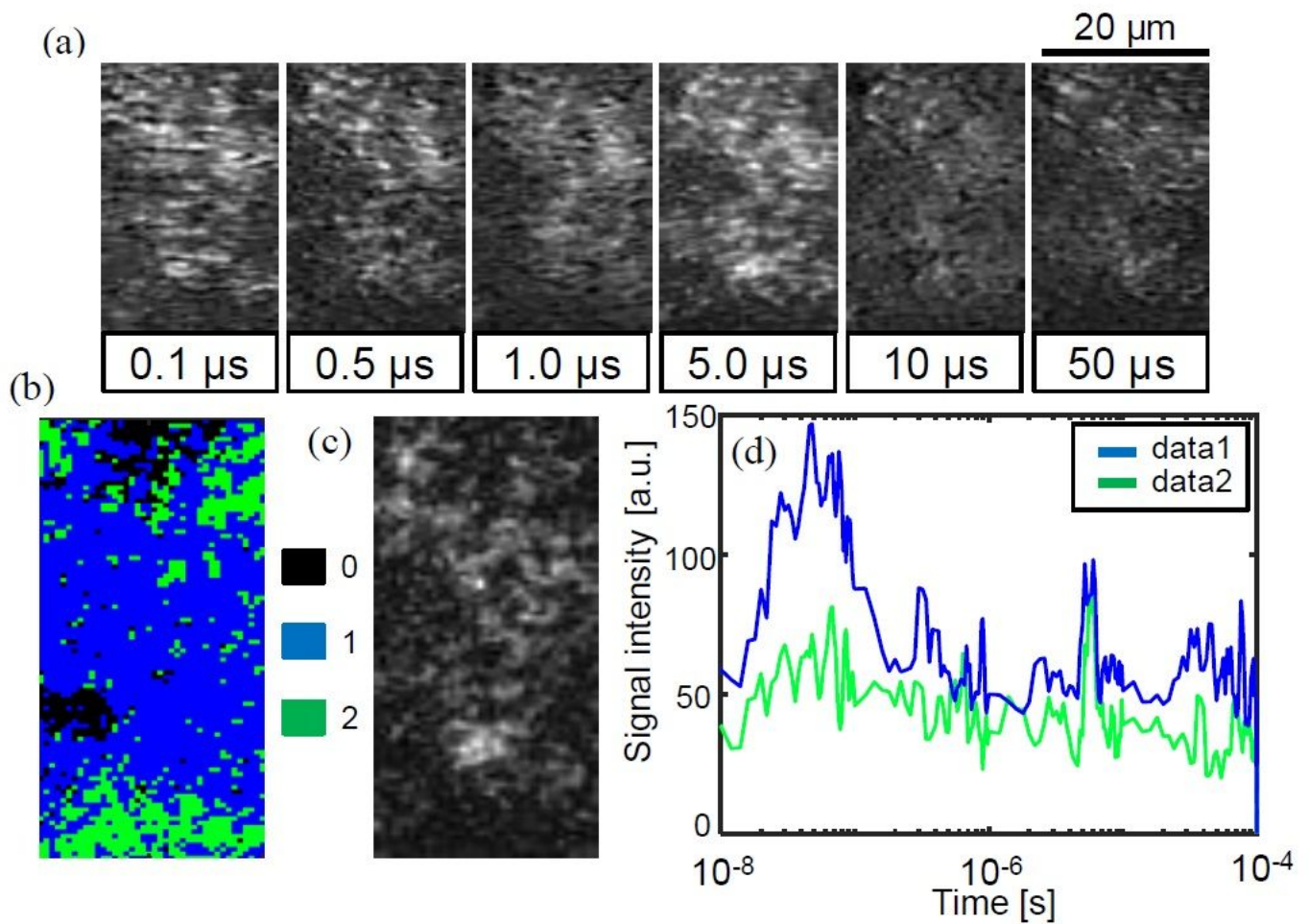


Figure 7

(a) An image sequence of the refractive index response for STOR/ITO/BVOM in water in a square region (20×50 μm) corresponding to No.1 on the order from nanoseconds to microseconds. The location of the sample was exactly the same as Fig.5(a). The scale bar corresponds to 20 μm. (b) The categorized mapping of the charge carrier responses of (a). An outlier positioned far from all categories was colored in black (#0) (c) A microscopic image in the same area as (a). (d) The averaged responses for each category in (b) are shown.

Supplementary Files

This is a list of supplementary files associated with this preprint. Click to download.

- [20210225SupportinginformationZscheme.pdf](#)